



Tracing concealed gold deposits using mercury isotopes in surface soils: A study from the Shuiyindong gold deposit, Guizhou province, China

Xuemin Liu ^a, Feilin Zhu ^{a,*}, Shuting Liu ^{a,*}, Qinping Tan ^b, Lin Wang ^c, Yue Yufan ^a, Lichen ^a

^a Applied Nuclear Techniques in Geosciences Key Laboratory of Sichuan Province, Chengdu University of Technology, Chengdu 610059, China

^b State Key Laboratory of Ore Deposit Geochemistry, Institute of Geochemistry, Chinese Academy of Sciences, Guiyang 550081, Guizhou, China

^c Rock and Mineral Testing Center of Henan Province, Zhengzhou 450012, China



ARTICLE INFO

Keywords:

Mineral exploration
Covered regions
Soil geochemistry
Geochemical dispersion
Hg isotope
Shuiyindong Au deposit

ABSTRACT

Surface soil sampling has been proved to be an effective and low-cost mineral exploration method in covered terrains. The critical question is to determine whether the surface anomalies originated from the mineralization at depth. Mercury isotope signatures have recently been employed as a tool for understanding the sources of Hg anomalies. Meanwhile, Hg is a traditional pathfinder for Au exploration. Can Hg isotopes be applied to trace the sources of Au anomalies in topsoils in covered areas? This is the first study that employed Hg isotopes as an exploration proxy for Au mineralization at depth. Surface soil samples over the concealed Shuiyindong Au deposit, China, were collected and their total Au (TAu), total Hg (THg) contents, and Hg isotope compositions were analyzed. Gold and Hg surface positive anomalies display high correlation indexes along the sampled traverse above the Shuiyindong Au deposit. Moreover, the Hg anomaly is significantly stronger than that of Au. Soils from deep ores-related areas show clearly positive $\delta^{202}\text{Hg}$ values (-0.78% to -0.23% , averaging $-0.46 \pm 0.19\%$, $n = 10$, 1SD) compared with those from the background areas (-1.67% to -0.66% , averaging $-1.07 \pm 0.28\%$, $n = 10$, 1SD). $\delta^{202}\text{Hg}$ and 1/THg in deep ores-related soils have been altered by the ascending geogas from the mineralized rocks of the Longtan Fm. Soil positive Au anomalies detected in the study area are sourced at depth in the Shuiyindong Au deposit. However, it is not feasible to apply $\Delta^{199}\text{Hg}$ to trace the anomalous Au sources in topsoils, because Hg(II) photoreduction can imprint the $\Delta^{199}\text{Hg}$ signature, leading to negative $\Delta^{199}\text{Hg}$ values in the soils. Semi-volatile Hg and ultra-fine Au particles are mobile and could continuously migrate from the depth to the surface through macro-structures and micro-fractures with the ascending geogas, then most of them are absorbed by the surface soils. Overall, this study successfully traced the Au deposit at >650 m depth using $\delta^{202}\text{Hg}$, which is significant for mineral exploration of deep-seated Au deposits, especially in unknown covered areas.

1. Introduction

The dramatically increasing demand for mineral resources has driven mineral exploration in regions covered by thick transported regolith, deeply weathered profiles, or rocks (e.g., [de Caritat et al., 2016](#); [González-Álvarez et al., 2016, 2020](#); [Louheed et al., 2020](#); [Momo et al., 2019](#); [Wang et al., 2016](#)). Novel techniques which collect various surface media to generate exploration targets of deep deposits in the covered areas (e.g., [Cameron et al., 2004](#); [Clarke and Meier, 1990](#); [Kelley, 2003](#); [Lintern et al., 2013](#); [Mann et al., 1998](#); [Wang et al., 1997](#); [Wang, 1998](#)) are theoretically promising because the potential mechanisms by which metals may transfer from the ores upwards and laterally through

unmineralized transported cover have been comprehensively studied (e.g., [Anand et al., 2016](#); [Aspandiar et al., 2006](#); [Cameron et al., 2004](#); [Kelley et al., 2006](#)). However, surface geochemical anomalies can be formed by diverse processes ([Cameron et al., 2004](#); [Cheng, 2007](#); [Cohen et al., 2010](#); [Grunsky and de Caritat, 2019](#); [Mann et al., 1998](#); [Rantitsch, 2001](#); [Spadoni, 2006](#); [Wang et al., 1997](#); [Yousefi et al., 2013](#)). One of the most challenging aspects of mineral exploration in covered regions is to discriminate which geochemical anomalies form as the result of vertical dispersion processes associated with the presence of ore deposits at depth and which geochemical anomalies are not sourced from ore deposits ([Chardon et al., 2018](#); [Cohen et al., 2010](#); [Wang et al., 2016](#); [Wang and Zuo, 2020](#)). Metal isotope tracing is a potential technique to detect

* Corresponding authors at: Chengdu University of Technology, Dongshan Road, Exianqiao, Chengdu 610059, China.

E-mail addresses: zhufeilin2012@cdut.edu.cn (F. Zhu), liushuting@zju.edu.cn (S. Liu).

the real footprint of buried ore deposits (reviewed by Kyser et al., 2020), but only the stable isotopes of Cu (Braxton and Mathur, 2011; Kidder et al., 2020; Mathur et al., 2009; Mathur et al., 2012) and U (Brennecke et al., 2010; Keegan et al., 2008; Uvarova et al., 2014) have been applied as tracers in mineral exploration.

Mercury is a traditional pathfinder for the geochemical exploration of gold deposits (Adepoju, 2019; Hedenquist et al., 2000; Korshunova and Charykova, 2019; McCarthy Jr., 1972; Sadeghi et al., 2015; Varekamp and Buseck, 1984; Wang et al., 2021; Yalali-Abanuz et al., 2012). Mercury isotope geochemistry has recently been employed as a tool for understanding the sources of Hg (Smith et al., 2005, 2008; Xu et al., 2018; Yin et al., 2016a), and perhaps Au anomalies in surface media in covered areas. Mercury has seven natural stable isotopes (^{196}Hg , ^{198}Hg , ^{199}Hg , ^{200}Hg , ^{201}Hg , ^{202}Hg , and ^{204}Hg), and they undergo both mass-dependent fractionation (MDF) and mass-independent fractionation (MIF), which provide multidimensional information about the sources and fates of Hg in the environment (reviewed by Blum et al., 2014). Hg-MDF occurs during most chemical (e.g., photoreduction, ligand exchange, sorption, precipitation, and abiotic methylation), physical (e.g., diffusion, evaporation, and volatilization), and biological processes (e.g., microbial methylation, demethylation) (e.g., Bergquist and Blum, 2007; Yin et al., 2010). Unlike Hg-MDF, Hg-MIF mainly occurs during photochemical reactions (Blum et al., 2014; Yin et al., 2010). A large variation of Hg-MDF and Hg-MIF signals has been reported in natural samples (e.g., Bergquist and Blum, 2007; Sherman et al., 2009; Sonke et al., 2010; Sun et al., 2013; Yin et al., 2013).

The Shuiyindong Au deposit, a known concealed deposit in Guizhou province, China, was taken as an example in this study. Its deep Au ore bodies are preferentially disseminated in bioclastic limestone and calcareous siltstone of the Upper Permian Longtan Fm at depths of 100 to 1400 m below the surface (Su et al., 2008; Tan et al., 2015a, 2015b; Xia, 2005). Previous studies showed that Au mineralization in this deposit had a close relationship with high Hg contents (Su et al., 2012; Tan et al., 2015a; Yin et al., 2019). We collected surface soils along the sampled traverse above the concealed Shuiyindong Au ore bodies (>650 m in depth) and analyzed their total Au (TAu), total Hg (THg) concentrations, and Hg isotope compositions, aiming to determine if Hg isotopes can be exploited as mineral exploration proxies to detect Au mineralization at depth in the Shuiyindong deposit and to suggest the use of Hg isotopes as new exploration vectors in the exploration tool kit of Au explorers globally.

2. Geological setting

The Shuiyindong Au deposit is located approximately 20 km northwest of Zhenfeng County in Guizhou province, China (Su et al., 2008; Xia, 2005). Its mining area has been divided into four sections along the Huijiabao anticline from west to east: Shuiyindong, Xionghuangyan, Bojitian, and Nayang (Fig. 1). Recent exploration and underground mining have revealed gold reserves of more than 290 t, with an average grade of 5 g/t (Liu et al., 2017), making Shuiyindong the largest Carlin-type gold deposit discovered to date in Guizhou province (Tan et al., 2015a). Detailed geological descriptions of the Shuiyindong deposit are available in Liang et al. (2020), Su et al. (2008, 2012), and Tan et al. (2015a, 2015b).

Sedimentary rocks in the Shuiyindong deposit mainly consist of bioclastic limestone, siltstone, and argillite of the Middle and Upper Permian and Lower Triassic ages (Su et al., 2008; Fig. 2). The Middle Permian Maokou Fm (P_2m) is a massive bioclastic limestone and is separated from Longtan Fm (P_3l) by an unconformity (SBT), consisting of silicified, brecciated argillite and limestone (Liu et al., 2014; Tan et al., 2019; Fig. 2). The P_3l , about 300 m thick in this deposit, has been divided into three units (Liu, 2001). The lower unit (P_3l^1) consists of thick-bedded calcareous siltstone that grades into a fine-grained sandstone at the top; the middle unit (P_3l^2) consists of silty argillite intercalated with thin beds of bioclastic limestone and coal seams; the upper unit (P_3l^3) includes calcareous siltstone, sandstone, and muddy and bioclastic limestone. The P_3l is overlain by the Upper Permian Changxing Fm (P_3c , bioclastic limestone intercalated with argillite) and Dalong Fm (P_3d , argillite), and the Lower Triassic Yelang Fm (lower unit: T_1y^1 , muddy limestone; middle unit: T_1y^2 , Oolitic limestone; upper unit: T_1y^3 , claystone) (Tan et al., 2017; Fig. 2). No felsic intrusive rocks (or dikes) are distributed in this deposit. The Late Permian alkali flood basalt is observed in its northwestern part. The Cretaceous lamprophyre dikes located in its east have been considered to be unrelated to the Au mineralization (Liang et al., 2020).

These strata overlying the P_2m were deformed into a nearly E-W-trending anticline, the Huijiabao anticline in Fig. 1, with approximately 20 km in length, 5 km in width, and limbs that dip 10 to 20° (Su et al., 2008, 2012). Geological exploration has indicated that strata-bound gold ore bodies are mainly distributed on the flanks of this anticline axis (Su et al., 2008; Fig. 1). Its limbs are cut by two reverse faults, F101 and F105 in Fig. 1, which strike nearly E-W and dip steeply to the north and south, respectively (Tan et al., 2017). F101 runs through the whole Shuiyindong deposit, while F105 is not developed in the Bojitian and Nayang sections (Figs. 1 and 2). These two reverse faults are also cut by a

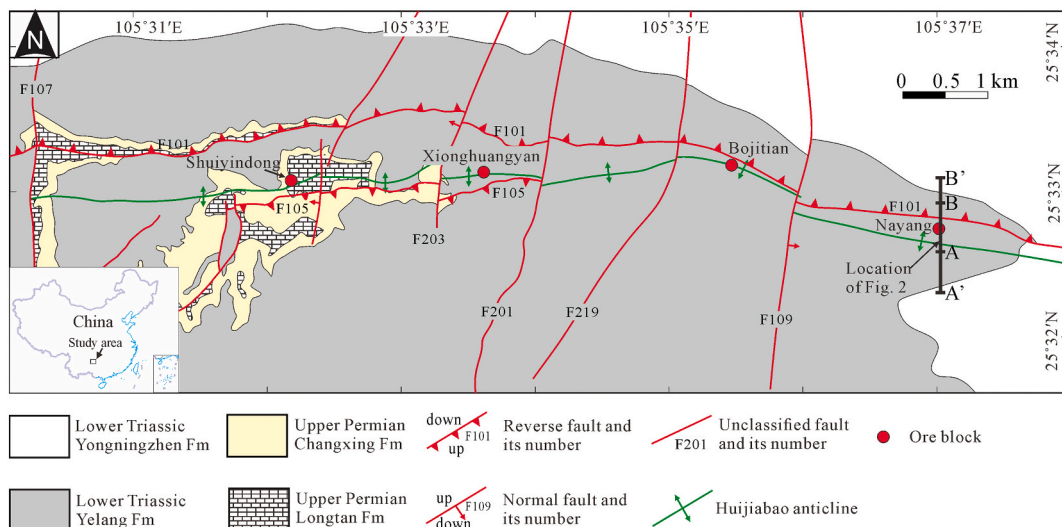


Fig. 1. Geological map of the Shuiyindong gold deposit (modified from Tan et al., 2019).

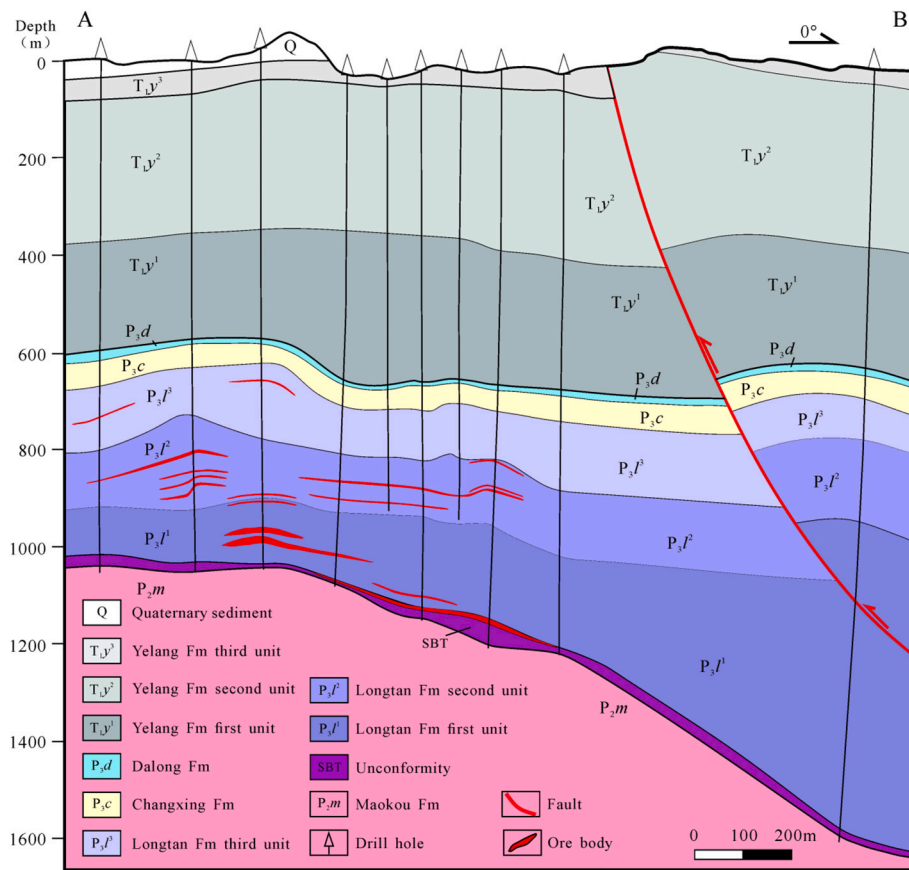


Fig. 2. Geological cross-section A-B through the Nayang section of the Shuiyindong gold deposit showing its major structures and stratigraphic units. The position of A-B is shown in Fig. 1.

series of near S–N trending strike-slip faults with steep dips (70–80°) (Su et al., 2008; Fig. 1).

Wallrock alteration types include decarbonatization, silicification, sulfidation, and dolomitization. Sulfides consist mainly of arsenian pyrite, arsenopyrite, marcasite, and lesser orpiment, realgar, and stibnite. Gangue minerals consist of quartz, dolomite, calcite, fluorite, and clay minerals (Su et al., 2008, 2012). The gold is mainly hosted in arsenian pyrite and arsenopyrite, mainly existing in the form of crystal lattice gold, submicroscopic particles, and nanoparticles (Liang et al., 2020; Su et al., 2008, 2012; Tan et al., 2019).

The Shuiyindong deposit is currently located on the south-eastwards margin of the Tibetan Plateau (Wang et al., 2020). The Au mineralization took place during the Late Jurassic to Early Cretaceous times (Sm–Nd isochron ages of 134–136 Ma for *syn*-ore hydrothermal calcite; Su et al., 2009). The intensified uplift of the Tibetan Plateau in the Cenozoic facilitated the development of an Asian Monsoon climate (An et al., 2001; Sun and Wang, 2005) and caused erosion and weathering in Shuiyindong (Guo et al., 2002; Li et al., 2007; Sun and Wang, 2005), resulting in a low-relief karst plain. The topsoil developed above the bedrock is mainly Red earth, Yellow earth, and lime soil (Gu et al., 2020; Liu et al., 2009).

3. Methods

3.1. Sample collection and preparation

The S–N A'-B' exploration line (Fig. 1) in the Nayang section is nearly perpendicular to the strike of the ore bodies and the Huijiabao anticline, with a total length of about 1354 m. The deep ore bodies under the A-B exploration line are controlled by 10 drilling holes (Fig. 2) and are mainly located in the Longtan Fm at depths of 650 to 1200 m below

the surface (Fig. 2). Twenty sampling sites were located at a spacing of 50–100 m along the A'-B' exploration line, including 8 sites above the concealed ore bodies and the F101 (A-B, Fig. 1) and 12 sites in the background areas (A-A' and B-B', Fig. 1). To avoid mining-related contamination, the sampling sites were located away from the mine adits, roads, tailings, lagoons, and the ore processing mill. At each site, one soil sample of around 1000 g was collected at a depth of 20–30 cm to avoid the organic horizon. Each sample was composed of generally 3 pits in the layout of an equilateral triangle within a 2 m interval. After fieldwork, soil samples were dried at room temperature, impurities were removed, and fine-grained soil of –200 mesh (76 µm) was sieved for analysis.

3.2. Laboratory analysis and data quality control

TAu and THg in soil samples were analyzed at the Rock and Mineral Testing Centre of Henan province, Zhengzhou, China. A 10.0 g fine-grained soil sample was decomposed by aqua regia [aqua regia (1HNO₃ + 3HCl): pure water = 1:1 vol.]. The Au in the solution was enriched by oscillating adsorption of foam plastic and then was thermally liberated with thiourea solution (10 g/L). The TAu in the solution was detected with XSeries2 Inductively Coupled Plasma-Mass Spectrometry. Another 1.0 g sample was digested with aqua regia [aqua regia (1HNO₃ + 3HCl): pure water = 1:1 vol.] in the boiling water bath, thus all the Hg contained entered the solution in the form of Hg²⁺, and then it was reduced to Hg⁰ with KBO₄ (2 g/L)-KOH (0.1 g/L) solution. The THg content in the solution was tested with Atomic Fluorescence Spectrophotometer. Detailed analyzed methods for the TAu and THg contents were in full accordance with Chinese National Standard methods, i.e., DZ/T 0279.4-2016 (Analysis methods for regional geochemical sample - Part 4: Determination of aurum contents by foamed plastic enrichment -

inductively coupled plasma mass spectrometry) and NY/T1121.10-2006 (Soil Testing, Part 10: Method for determination of soil total hydrgyrum), respectively.

The detection limits of TAu and THg were 0.15 ppb and 0.5 ppb, respectively, and their proportions of reportable values were both 100%. Two standards were inserted into these 20 soil samples for accuracy and precision control. i.e., GAu-9 (RSD = 7.98%, n = 1) and GAu-11 (RSD = 3.98%, n = 1) for TAu (Yan et al., 1995), GSS-19 (RSD = 16.71%, n = 1) and GSS-23 (RSD = 1.16%, n = 1) for THg (<https://www.ncrm.org.cn/Web/Ordering/MaterialDetail?autoID=7456>; <https://www.ncrm.org.cn/Web/Ordering/MaterialDetail?autoID=7460>). High-quality TAu and THg data were obtained.

Mercury isotopic compositions were analyzed at the Institute of Geochemistry, Chinese Academy of Sciences, Guiyang, China. Soil samples were prepared for mercury isotope analysis following the double-stage thermal combustion and pre-concentration protocol (see the detailed method in Zerkle et al., 2020). The prepared samples were diluted to 1 ng/mL Hg and measured by a Neptune Plus multi-collector inductively coupled plasma mass spectrometer, following the method by Yin et al. (2016b). Mercury concentrations and acid matrices in the bracketing NIST-3133 solutions were matched well with the neighboring samples. Mercury isotopic compositions were reported following the convention recommended by Blum and Bergquist (2007). Specifically, MDF is expressed in δ notation in units of ‰ referenced to the NIST-3133 Hg standard (analyzed before and after each sample):

$$\delta^{\text{xxx}}\text{Hg} (\text{‰}) = [(\text{xxxHg}/{}^{198}\text{Hg}_{\text{sample}})/(\text{xxxHg}/{}^{198}\text{Hg}_{\text{standard}}) - 1] \times 1000$$

where xxx = 199, 200, 201, and 202.

MIF is reported in Δ notation in units of ‰, which describes the difference between the measured $\delta^{\text{xxx}}\text{Hg}$ and the theoretically predicted $\delta^{\text{xxx}}\text{Hg}$ value:

$$\Delta^{\text{xxx}}\text{Hg} \approx \delta^{\text{xxx}}\text{Hg} - \delta^{\text{202}}\text{Hg} \times \beta$$

β is equal to 0.2520 for ${}^{199}\text{Hg}$, 0.5024 for ${}^{200}\text{Hg}$, and 0.7520 for ${}^{201}\text{Hg}$. Analytical uncertainty was estimated based on the replication of the NIST-3177 standard solution. The overall average and uncertainty of NIST-3177 ($\delta^{\text{202}}\text{Hg}$: $-0.47 \pm 0.00\text{‰}$; $\Delta^{\text{199}}\text{Hg}$: $-0.005 \pm 0.01\text{‰}$; $\Delta^{\text{201}}\text{Hg}$: $-0.05 \pm 0.11\text{‰}$; 2SD, n = 2) agree well with comparable previous studies (Blum and Bergquist, 2007).

4. Results

TAu and THg concentrations, and Hg isotope compositions of 20 surface soil samples are shown in Table 1. It must be noted in advance that when we collected samples in the field, twenty sampling sites were located along the A'-B' exploration line (Fig. 1), including 8 sites above the concealed ore bodies and the F101 (A-B in Fig. 1; 10 drilling holes in Fig. 2 control this area) and 12 sites in areas without drilling hole control (A-A' and B-B' in Fig. 1). The latter was originally thought to be background areas. However, our results show that there might be deep blind ore bodies under sampling points 19 and 20, which will be discussed in detail in the following. Therefore, there are 10 samples above the deep concealed ore bodies and the F101 (hereinafter deep ores-related soils; Sample ID of 6-13, 19, and 20 in Table 1) and 10 samples in the background areas (hereinafter background soils; Sample ID of 1-5 and 14-18 in Table 1).

4.1. Total Au and Hg concentrations

Table 2 lists TAu and THg parameters for all 20 samples, 10 background soils, and 10 deep ores-related soils. TAu and THg of all soil samples are 0.93 to 5.55 ppb (with an average of 2.84 ppb) and 0.217 to 11.884 ppm (with an average of 2.483 ppm), respectively. Their coefficient of variation (CV) values are 136% and 44%, respectively, indicating that the variations of THg contents among 20 samples are much greater than those of TAu. Bivariate correlation analysis shows a strong positive relationship between TAu and THg (Pearson correlation coefficient: 0.720, Table 3), and the correlation is significant at the 0.01 level (two-tailed test).

TAu concentrations differ between background (0.93–2.94 ppb) and deep ores-related (1.88–5.55 ppb) samples. The median, arithmetic mean (AM), and geometric mean (GM) of TAu for the deep ores-related soils are 1.59, 1.70, and 1.69 times those of the background soils, respectively (Table 2). THg contents vary greatly between background (0.217–1.124 ppm) and deep ores-related (1.192–11.884 ppm) samples. And the median, AM, and GM of THg for the deep ores-related samples are 6.13, 7.08, and 6.61 times those for the background samples (Table 2). TAu and THg of soils above the mining area are much higher than those above the non-mining area.

As can be seen from Fig. 3, the change trends of TAu and THg along the A'-B' exploration line are relatively consistent, and there are obvious

Table 1

Total digestion results of Au and Hg (TAu in ppb, THg in ppm), and Hg isotopic compositions (‰) of surface soil samples collected along the A'-B' exploration line in the Nayang section of the Shuiyindong gold deposit.

Sample ID	Position	TAu	THg	$\delta^{\text{202}}\text{Hg}$	$\delta^{\text{201}}\text{Hg}$	$\delta^{\text{200}}\text{Hg}$	$\delta^{\text{199}}\text{Hg}$	$\Delta^{\text{201}}\text{Hg}$	$\Delta^{\text{200}}\text{Hg}$	$\Delta^{\text{199}}\text{Hg}$
1	B	2.87	0.282	-1.12	-1.04	-0.58	-0.49	-0.20	-0.02	-0.20
2		1.85	0.224	-1.67	-1.53	-0.87	-0.75	-0.28	-0.03	-0.33
3		2.94	1.080	-0.95	-0.87	-0.46	-0.38	-0.16	0.02	-0.14
4		2.02	0.685	-1.20	-1.14	-0.57	-0.40	-0.24	0.03	-0.09
5		2.89	1.124	-0.66	-0.70	-0.35	-0.29	-0.20	-0.02	-0.12
6		4.39	3.566	-0.41	-0.45	-0.20	-0.20	-0.14	0.01	-0.10
7		3.25	2.724	-0.57	-0.50	-0.31	-0.29	-0.07	-0.03	-0.15
8		2.35	1.307	-0.78	-0.80	-0.41	-0.41	-0.21	-0.02	-0.21
9	A	1.88	1.192	-0.69	-0.69	-0.39	-0.33	-0.17	-0.04	-0.16
10		5.55	3.377	-0.50	-0.50	-0.21	-0.19	-0.13	0.04	-0.06
11		5.33	11.719	-0.33	-0.31	-0.15	-0.09	-0.06	0.01	-0.01
12		4.20	11.884	-0.23	-0.18	-0.12	-0.13	-0.01	-0.01	-0.07
13		3.42	3.207	-0.54	-0.48	-0.29	-0.23	-0.07	-0.02	-0.10
14		1.38	0.217	-1.16	-1.02	-0.65	-0.49	-0.15	-0.06	-0.19
15		2.24	1.090	-0.76	-0.78	-0.39	-0.39	-0.21	-0.01	-0.20
16	B	1.83	0.261	-1.24	-1.06	-0.62	-0.41	-0.13	0.01	-0.10
17		2.17	0.956	-0.90	-0.80	-0.40	-0.37	-0.12	0.06	-0.14
18		0.93	0.232	-1.05	-0.97	-0.52	-0.43	-0.18	0.01	-0.17
19	A	2.32	2.656	-0.24	-0.24	-0.04	-0.03	-0.07	0.08	0.03
20		3.15	1.879	-0.33	-0.37	-0.13	-0.19	-0.12	0.03	-0.11

Note: B - samples in the background areas (hereinafter background soils); A - samples above the deep concealed ore bodies and the F101 (hereinafter deep ores-related soils).

Table 2

Statistical parameters of the TAu and THg of surface soil samples collected along the A'-B' exploration line in the Nayang section of the Shuiyindong gold deposit.

Elements		Min.	Median	Max.	AM	GM	SD	CV
TAu (ppb)	Total (n = 20)	0.93	2.61	5.55	2.84	2.60	1.24	44%
	B (n = 10)	0.93	2.10	2.94	2.11	2.00	0.66	31%
	A (n = 10)	1.88	3.34	5.55	3.58	3.38	1.26	35%
	Enrichment coefficient	–	1.59	–	1.70	1.69	–	–
THg (ppm)	Total (n = 20)	0.217	1.157	11.884	2.483	1.247	3.372	136%
	B (n = 10)	0.217	0.484	1.124	0.615	0.485	0.410	67%
	A (n = 10)	1.192	2.966	11.884	4.351	3.204	4.011	92%
	Enrichment coefficient	–	6.13	–	7.08	6.61	–	–

Note: total - 20 soil samples; B - 10 background soil samples; A - 10 deep ores-related soil samples; Min. - minimum; Max. - maximum; AM - arithmetic mean; GM - geometric mean; SD - standard deviation; CV - coefficient of variation = (SD/AM) × 100%; enrichment coefficient = value of A/value of B (value: median, AM or GM).

Table 3

Pearson correlation coefficients between TAu, THg, and Hg isotopic compositions of 20 surface soils along the A'-B' exploration line in the Nayang section of the Shuiyindong gold deposit.

	THg	$\delta^{202}\text{Hg}$	$\delta^{201}\text{Hg}$	$\delta^{200}\text{Hg}$	$\delta^{199}\text{Hg}$	$\Delta^{201}\text{Hg}$	$\Delta^{200}\text{Hg}$	$\Delta^{199}\text{Hg}$
TAu	0.720**	0.654**	0.655**	0.649**	0.639**	0.519*	0.192	0.523*
THg		0.646**	0.684**	0.622**	0.647**	0.701**	0.074	0.547*
$\delta^{202}\text{Hg}$			0.991**	0.988**	0.947**	0.748**	0.305	0.727**
$\delta^{201}\text{Hg}$				0.980**	0.956**	0.829**	0.309	0.756**
$\delta^{200}\text{Hg}$					0.965**	0.738**	0.447*	0.780**
$\delta^{199}\text{Hg}$						0.790**	0.473*	0.908**
$\Delta^{201}\text{Hg}$							0.242	0.710**
$\Delta^{200}\text{Hg}$								0.615**

Note: * - Correlation coefficients significant at the 0.05 level (two-tailed test); ** - Correlation coefficients significant at the 0.01 level (two-tailed test).

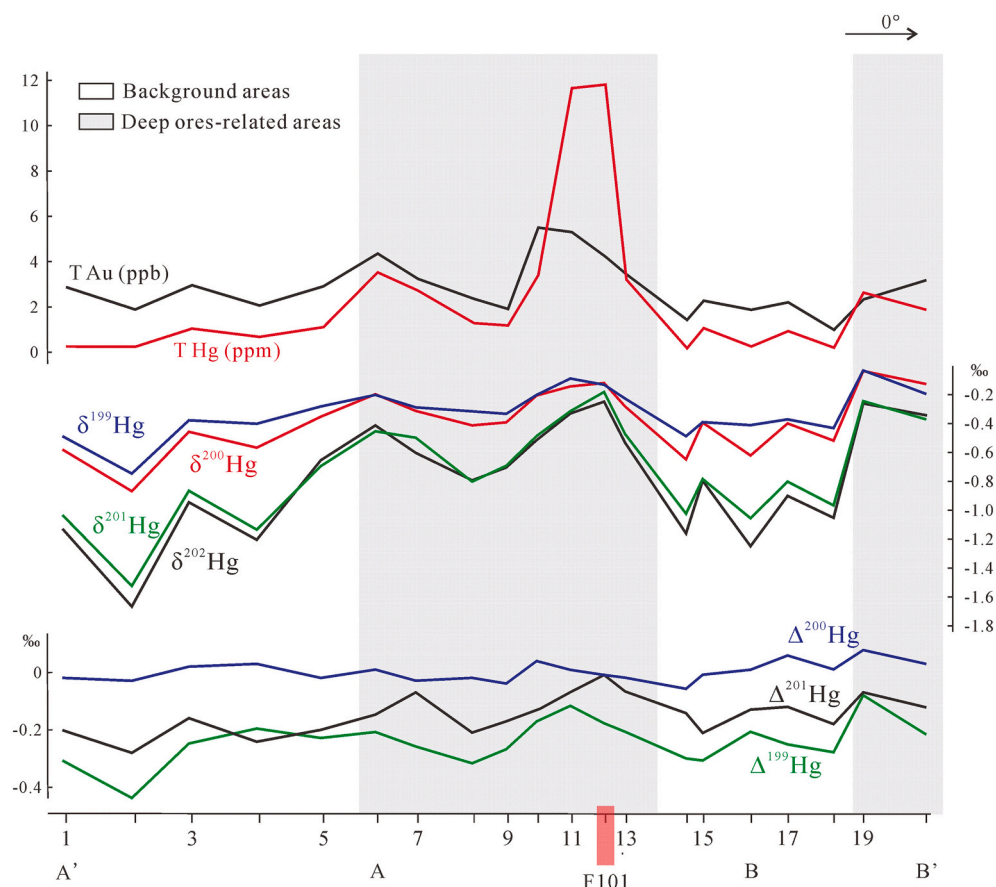


Fig. 3. Change trends of TAu, THg, and Hg isotopic compositions of surface soils along the A'-B' exploration line in the Nayang section of the Shuiyindong gold deposit. The location of A'-A-B-B' is shown in Fig. 1. The distribution of deep Au ore bodies and F101 under the A-B line is shown in Fig. 2. The red rectangle around the point of 12 is the F101 outcrop on the surface. Under points of No. 19 and No. 20, it's speculated that deep ores bodies are distributed.

anomalies above the ore bodies (points No. 6, No. 10, and No. 11) and the F101 (No. 12). The strongest anomaly occurs around points of No. 10 (5.55 ppb) and No. 11 (5.33 ppb) for TAu, and around points of No. 11 (11.719 ppm) and No. 12 (11.884 ppm) for THg.

4.2. Mercury isotopic compositions

Table 4 lists statistical parameters of Hg isotope signatures for all 20 samples, 10 background samples, and 10 deep ores-related samples. The $\delta^{202}\text{Hg}$ and $\Delta^{199}\text{Hg}$ values of all samples range from $-1.67\text{\textperthousand}$ to $-0.23\text{\textperthousand}$, with an average of $-0.77 \pm 0.39\text{\textperthousand}$ ($n = 20$, 1SD), and from $-0.33\text{\textperthousand}$ to $0.03\text{\textperthousand}$, with an average of $-0.13 \pm 0.08\text{\textperthousand}$ ($n = 20$, 1SD), respectively. Hg-MDF and odd Hg-MIF are significant, given the 2SD analytical uncertainty of $\delta^{202}\text{Hg}$ ($\pm 0.00\text{\textperthousand}$) and $\Delta^{199}\text{Hg}$ ($\pm 0.01\text{\textperthousand}$). No significant even Hg-MIF ($\Delta^{200}\text{Hg}$) is shown for all soils in our study ($\Delta^{200}\text{Hg}$ of $-0.06\text{\textperthousand}$ to $0.08\text{\textperthousand}$, averaging $0.00 \pm 0.03\text{\textperthousand}$, $n = 20$, 1SD) (**Table 4**).

$\delta^{202}\text{Hg}$ values differ between background ($-1.67\text{\textperthousand}$ to $-0.66\text{\textperthousand}$, averaging $-1.07 \pm 0.28\text{\textperthousand}$, $n = 10$, 1SD) and deep ores-related soils ($-0.78\text{\textperthousand}$ to $-0.23\text{\textperthousand}$, averaging $-0.46 \pm 0.19\text{\textperthousand}$, $n = 10$, 1SD), and the former is obviously lower than the latter. However, there is no clear difference in $\Delta^{199}\text{Hg}$ between background and deep ores-related soils. $\Delta^{199}\text{Hg}$ values in background and deep ores-related soils range from $-0.30\text{\textperthousand}$ to $-0.10\text{\textperthousand}$ (average: $-0.17 \pm 0.07\text{\textperthousand}$, $n = 10$, 1SD) and $-0.20\text{\textperthousand}$ to $0.00\text{\textperthousand}$ (average: $-0.09 \pm 0.07\text{\textperthousand}$, $n = 10$, 1SD), respectively.

The absolute CV values of $\delta^{202}\text{Hg}$, $\delta^{201}\text{Hg}$, $\delta^{200}\text{Hg}$, $\delta^{199}\text{Hg}$, $\Delta^{201}\text{Hg}$, and $\Delta^{199}\text{Hg}$ for all soil samples are around 50%. The AM values of all seven Hg isotope signatures, and the median values of six signatures (except $\Delta^{200}\text{Hg}$) in background soils are slightly lower than those of deep ores-related soils. The ranges for MDF signatures in the deep ores-related soils are all smaller than those in the background soils, while their ranges for MIF signatures are equal. Slight or obvious positive correlations (Pearson correlation coefficients: 0.547–0.701, **Table 3**) are observed between THg and isotope compositions (except $\Delta^{200}\text{Hg}$), and strong positive correlations (Pearson correlation coefficients:

0.727–0.908, **Table 3**) are observed between Hg-MDF and odd Hg-MIF.

The change trends of Hg-MDF ($\delta^{202}\text{Hg}$, $\delta^{201}\text{Hg}$, $\delta^{200}\text{Hg}$, and $\delta^{199}\text{Hg}$) along the A'-B' exploration line are relatively consistent (**Fig. 3**), and there are obvious anomalies above the ore bodies (points of No. 6, No. 10 and No. 11) and the F101 (No. 12). Strong $\Delta^{199}\text{Hg}$ anomalies occur at points No. 6 and No. 11, and $\Delta^{201}\text{Hg}$ anomalies at points No. 7 and No. 12, which corresponded well with the deep Au ore bodies and the F101. Noticeably, the point of No. 19 shows significant anomalies of Hg isotope compositions and the weak THg anomaly, and the point of No. 20 has a slight TAu anomaly. There was no drilling control in this area, and it can be speculated that these comprehensive anomalies were likely induced by the deep blind ore bodies (no faulting structures exist in this area based on the fieldwork).

5. Discussion

5.1. Anomalous TAu and THg in surface soils

There are obvious TAu anomalies in deep ores-related samples (**Table 2**; **Fig. 3**), indicating that TAu of the surface soils can give a good indication of deep Au mineralization in the covered areas. Several previous studies have obtained similar results. For example, in the Yueyang Bitian epithermal Ag-Au-U ore deposit, southeastern China, the anomalous Au, and Ag distribution in the soils by near-total digestion coincided well with its concealed deposit ([Zhang et al., 2015](#)). And in the Jinwozi goldfield, a significant N-E-trending Au anomaly delineated by total digestion of topsoils was coincident with the ductile-shear zone hosting the Au deposit ([Wang et al., 2007, 2016](#)).

THg and TAu in surface soils are closely related based on their strong positive relationship (Pearson correlation coefficient: 0.720; **Table 3**) and their relatively consistent change trends along the A'-B' exploration line (**Fig. 3**). Both THg and TAu of soils above the mining area are much higher than those above the non-mining area. However, the characteristics of anomalies for these two elements are not the same. THg contents of all soil samples (range: 0.217 to 11.884 ppm; **Table 2**) are larger than

Table 4

Statistical parameters (%) of Hg isotopic compositions of surface soil samples collected along the A'-B' exploration line in the Nayang section of the Shuiyindong gold deposit.

Hg isotopic composition	Min.	Median	Max.	Range	AM	SD	CV	
$\delta^{202}\text{Hg}$	Total ($n = 20$)	-1.67	-0.73	-0.23	1.44	-0.77	0.39	-51%
	B ($n = 10$)	-1.67	-1.09	-0.66	1.01	-1.07	0.28	-26%
	A ($n = 10$)	-0.78	-0.46	-0.23	0.55	-0.46	0.19	-40%
	A - B	-	0.63	-	-0.46	0.61	-	-
$\delta^{201}\text{Hg}$	Total ($n = 20$)	-1.53	-0.74	-0.18	1.35	-0.72	0.35	-48%
	B ($n = 10$)	-1.53	-1.00	-0.70	0.83	-0.99	0.24	-24%
	A ($n = 10$)	-0.80	-0.47	-0.18	0.62	-0.45	0.19	-42%
	A - B	-	0.53	-	-0.21	0.54	-	-
$\delta^{200}\text{Hg}$	Total ($n = 20$)	-0.87	-0.39	-0.04	0.83	-0.38	0.21	-55%
	B ($n = 10$)	-0.87	-0.55	-0.35	0.52	-0.54	0.15	-29%
	A ($n = 10$)	-0.40	-0.21	0.00	0.40	-0.23	0.12	-54%
	A - B	-	0.34	-	-0.12	0.31	-	-
$\delta^{199}\text{Hg}$	Total ($n = 20$)	-0.75	-0.35	-0.03	0.72	-0.32	0.17	-51%
	B ($n = 10$)	-0.75	-0.41	-0.29	0.46	-0.44	0.12	-28%
	A ($n = 10$)	-0.40	-0.20	0.00	0.40	-0.21	0.11	54%
	A - B	-	0.21	-	-0.06	0.23	-	-
$\Delta^{201}\text{Hg}$	Total ($n = 20$)	-0.28	-0.15	-0.01	0.27	-0.15	0.07	-47%
	B ($n = 10$)	-0.30	-0.19	-0.10	0.20	-0.19	0.05	-27%
	A ($n = 10$)	-0.21	-0.10	-0.01	0.20	-0.11	0.06	-57%
	A - B	-	0.09	-	0.00	0.08	-	-
$\Delta^{200}\text{Hg}$	Total ($n = 20$)	-0.06	0.00	0.08	0.14	0.00	0.03	1737%
	B ($n = 10$)	-0.06	0.00	0.06	0.12	0.00	0.03	-3414%
	A ($n = 10$)	-0.04	0.00	0.08	0.12	0.01	0.04	738%
	A - B	-	0.00	-	0.00	0.01	-	-
$\Delta^{199}\text{Hg}$	Total ($n = 20$)	-0.33	-0.13	0.03	0.36	-0.13	0.08	-60%
	B ($n = 10$)	-0.30	-0.16	-0.10	0.20	-0.17	0.07	-41%
	A ($n = 10$)	-0.20	-0.10	0.00	0.20	-0.09	0.07	-76%
	A - B	-	0.06	-	0.00	0.08	-	-

Note: total, B, A, Min., Max., AM, SD, and CV have the same meaning as explained in **Table 2**; range = Max. - Min; A - B = value of A - value of B (value: median, range, AM).

its upper limit of the background range of topsoils in Guizhou province (0.0212 ppm; Wang et al., 2015). But THg still varies greatly between deep ores-related and background samples (their ratios for the median, AM, and GM are 6.13, 7.08, and 6.61, respectively; Table 2), and the maximum THg of the latter (1.124 ppm) is smaller than the minimum Hg of the former (1.192 ppm). It indicates that the surface soils in the Shuiyindong deposit have generally higher THg concentrations compared to its background range in Guizhou, but the THg anomalies in deep ores-related samples are more significant than those in background samples. However, TAu contents of 3 deep ores-related samples and 7 background samples are smaller than its upper limit of the background range of topsoils in Guizhou province (2.86 ppb; Wang and the CGB sampling Team, 2015), and TAu also differ between deep ores-related and background samples, but with smaller ratios for the median, AM, and GM (1.59, 1.70, and 1.69, respectively; Table 2) compared to the THg. Thus, the intensity and distribution of TAu anomalies in soils are smaller than those of THg in the Shuiyindong deposit. Yin et al. (2019) also found a broad geochemical halo of Hg occurs in mineralized rocks ($\text{Au} > 0.10 \text{ ppm}$) and barren rocks ($\text{Au} < 0.05 \text{ ppm}$) from the Upper Permian Longtan Fm (mainly altered limestone and calcareous siltstone) in the Shuiyindong deposit, with Hg levels 2 to 3 orders of magnitude higher than that in other strata (mainly unaltered limestone). Therefore, compared to TAu, THg anomalies in surface soils are easier to detect and THg has a better effect in indicating deep concealed Au mineralization in this study.

5.2. Tracing anomalous THg and TAu in surface soils using Hg-MDF isotopes

Hg-MDF isotopes ($\delta^{202}\text{Hg}$, $\delta^{201}\text{Hg}$, $\delta^{200}\text{Hg}$, and $\delta^{199}\text{Hg}$) show strong positive correlations (Pearson correlation coefficients: 0.947–0.991; Table 3) and relatively consistent change trends along the A'-B' exploration line (Fig. 3), so Hg-MDF will be discussed in terms of $\delta^{202}\text{Hg}$. $\delta^{202}\text{Hg}$ values of soil samples vary from $-1.67\text{\textperthousand}$ to $-0.23\text{\textperthousand}$ with an average of $-0.77 \pm 0.39\text{\textperthousand}$ ($n = 20$, 1SD) (Table 4), within the range previously reported for soil samples from different sites of the world ($-5.0\text{\textperthousand}$ to $1.0\text{\textperthousand}$, summarized by Blum et al., 2014). Soils from deep ores-related areas ($-0.78\text{\textperthousand}$ to $-0.23\text{\textperthousand}$, averaging $-0.46 \pm 0.19\text{\textperthousand}$, $n = 10$, 1SD) show obviously positive $\delta^{202}\text{Hg}$ values compared to those from the background areas ($-1.67\text{\textperthousand}$ to $-0.66\text{\textperthousand}$, averaging $-1.07 \pm 0.28\text{\textperthousand}$, $n = 10$, 1SD) (Fig. 4; Table 4). Yin et al. (2019) systematically collected sedimentary rock samples in the Shuiyindong deposit and analyzed their Hg isotopic compositions. The mineralized rocks ($\text{Au} > 0.10 \text{ ppm}$) in the Longtan Fm have mean $\delta^{202}\text{Hg}$ of $0.05 \pm 0.53\text{\textperthousand}$ (1SD, $n = 56$), slightly higher ($p < 0.05$, t -test) than that of barren rocks ($\text{Au} < 0.05 \text{ ppm}$) in the Longtan Fm ($-0.73 \pm 0.99\text{\textperthousand}$, 1SD, $n = 51$) but much higher ($p < 0.01$, t -test) than that of barren rocks ($\text{Au} < 0.05 \text{ ppm}$) in other strata ($-1.38 \pm 0.56\text{\textperthousand}$, 1SD, $n = 62$) (Yin et al., 2019). As shown in Fig. 4, the $\delta^{202}\text{Hg}$ values of deep ores-related soils are more similar to those of the mineralized rocks ($\text{Au} > 0.10 \text{ ppm}$) in the Longtan Fm, whereas the $\delta^{202}\text{Hg}$ values of background soils are more similar to those of the rocks from the Yelang Fm, the parent rocks of the topsoils (Fig. 2). The $\delta^{202}\text{Hg}$ of total gaseous mercury in Guizhou province is $-0.65 \pm 0.37\text{\textperthousand}$ (1SD, $n = 46$) (Yu et al., 2016; Fig. 4), similar to that of soil samples in our study.

Mercury isotopic compositions in topsoils can be explained by the mixing of Hg from different sources (e.g., weathered rocks, dry and wet precipitation, and ascending geogas) and/or isotope fractionation during Hg cycling in the soil system, including microbial (e.g., micro reduction, methylation/demethylation) and abiotic (e.g., photoreduction, volatilization, evaporation, adsorption, and leaching) processes (e.g., Jiskra et al., 2017; Zheng et al., 2016). Because 20 soils in this study collected along the A'-B' exploration line (Fig. 1) developed under similar physical, chemical, and microbial conditions, the $\delta^{202}\text{Hg}$ difference between deep ores-related and background soils caused by Hg isotope fractionation in the soil system, even if it exists, can be ignored. These 20 soils share the common primary (weathered) rocks (the Yelang

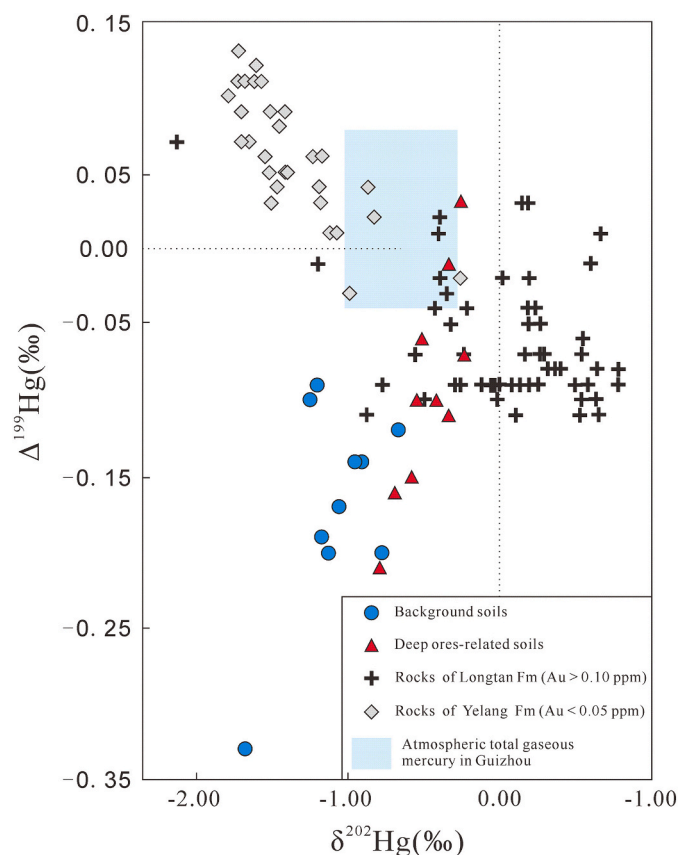


Fig. 4. Plot of $\Delta^{199}\text{Hg}$ versus $\delta^{202}\text{Hg}$ for soils and rocks from the Shuiyindong Au deposit. The 2SD analytical uncertainty values of $\delta^{202}\text{Hg}$ and $\Delta^{199}\text{Hg}$ for soils in this study are $\pm 0.00\text{\textperthousand}$ and $\pm 0.01\text{\textperthousand}$, respectively. The rocks' data is from Yin et al. (2019), and the 2SD analytical uncertainty values of $\delta^{202}\text{Hg}$ and $\Delta^{199}\text{Hg}$ for rocks are $\pm 0.11\text{\textperthousand}$ and $\pm 0.06\text{\textperthousand}$, respectively. Atmospheric total gaseous mercury in Guizhou province shows negative $\delta^{202}\text{Hg}$ and near-zero $\Delta^{199}\text{Hg}$ ($\delta^{202}\text{Hg}$, $-0.65 \pm 0.37\text{\textperthousand}$; $\Delta^{199}\text{Hg}$, $0.02 \pm 0.06\text{\textperthousand}$; 1SD; $n = 46$) (Yu et al., 2016).

Fm; Fig. 2) and dry and wet precipitation. Thus, the most likely cause of the $\delta^{202}\text{Hg}$ difference between deep ores-related and background soils is the geogas from the deep.

The geogas is defined as an ascending gas flow containing N_2 , O_2 , CO_2 , CO , CH_4 , NH_3 , and inert gases released from degassing of the upper mantle and lithosphere to the earth's surface (Annunziatelli et al., 2003; Cao et al., 2009; Gold and Soter, 1980; Malmqvist and Kristiansson, 1984; Morner and Etiope, 2002; Tong et al., 1998). It can carry ultra-fine metal particles, as well as semi-volatile Hg, from concealed ore bodies or other geological bodies and transport them to the earth's surface (Wang et al., 1995, 1997). Soil serves as a shielding layer for the diffusion from the underground to the air. Previous studies showed that Au mineralization in this deposit had a close relationship with high Hg contents (Su et al., 2012; Tan et al., 2015a; Yin et al., 2019). Therefore, Hg concentrations and Hg isotope compositions in the geogas should differ from deep ores-related areas to wall rocks.

A linear correlation between $\delta^{202}\text{Hg}$ and $1/\text{THg}$ is observed for our soils (Fig. 5), indicating the mixing of two Hg sources. The Yelang Fm is the primary rock of soils (Fig. 2), so Hg sources from the Yelang Fm fit well as an end member for this correlation line (Fig. 5). We predict the other end-member is Hg-containing geogas from the mineralized rocks of the Longtan Fm. $\delta^{202}\text{Hg}$ and $1/\text{THg}$ in deep ores-related soils have been altered by the ascending geogas from the mineralized rocks of the Longtan Fm. Thus, THg anomalies in surface soils could be traced from the deep Au mineralization using Hg-MDF ($\delta^{202}\text{Hg}$). Since THg and TAu in surface soils are closely related (Table 3; Fig. 3), Hg-MDF ($\delta^{202}\text{Hg}$)

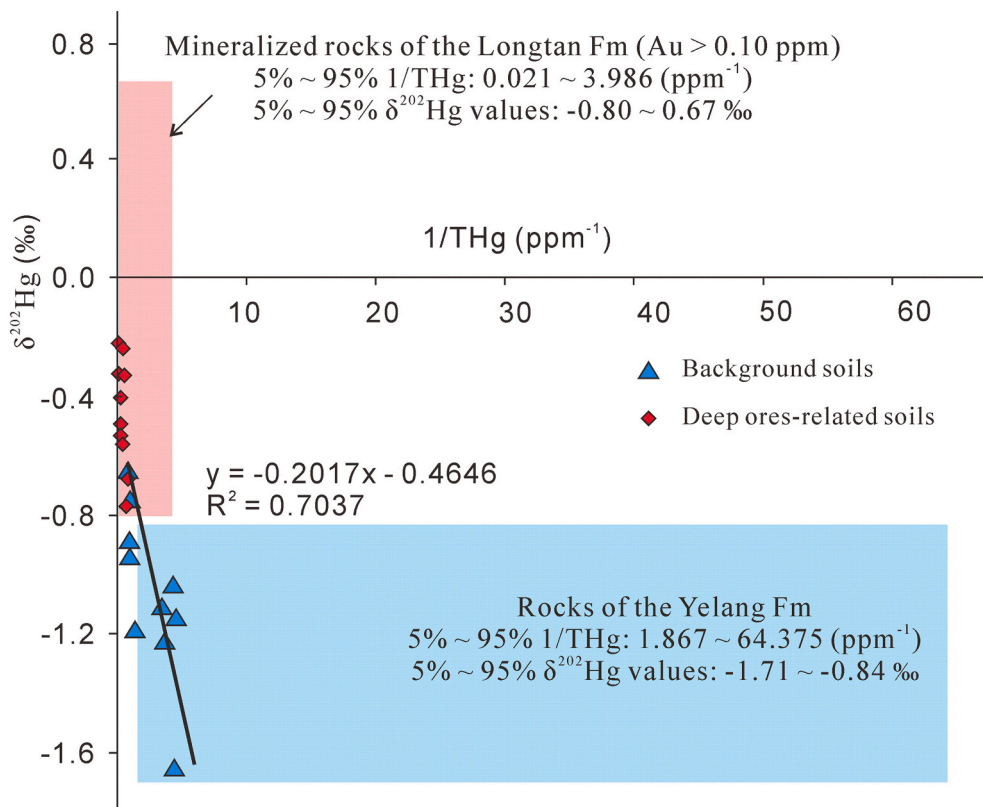


Fig. 5. $\delta^{202}\text{Hg}$ (‰) versus $1/\text{THg}$ (ppm^{-1}) for soils indicates a binary mixing of rocks of the Yelang Fm and mineralized rocks of the Longtan Fm ($\text{Au} > 0.10 \text{ ppm}$). $\delta^{202}\text{Hg}$ and THg values of rocks were referred from Yin et al. (2019). “5%–95%” means the 5% quantile to 95% quantile.

also could indicate anomalous Au sources in topsoils from the deep Au ore bodies in this study.

The climate in the Shuiyindong is warm and moist, with an annual average temperature between 18.4 and 19.5 °C, and an annual average relative humidity of 81%, and the vegetation there is flourishing (Gu et al., 2020; Liu et al., 2009). The litterfall could influence the Hg-MDF of the soils. Background soils in forest areas are largely altered by the negative MDF (3‰ to 1‰) during adsorption of $\text{Hg}(0)$ by foliage (Demers et al., 2013; Zheng et al., 2016). The more negative $\delta^{202}\text{Hg}$ in soils can be greatly attributed to the inputs of litterfall which favors adsorption of isotopically light $\text{Hg}(0)$ by foliage (Demers et al., 2013; Zheng et al., 2016). However, the difference in $\delta^{202}\text{Hg}$ values between soils in this study and their weathered rocks (the Yelang Fm, Fig. 4) is not so significant, which might be explained by the sampling depth, i.e., 20–30 cm to avoid organic horizon. Low biomass density causes less adsorption of isotopically light Hg by vegetation cover.

5.3. Tracing anomalous THg and TAu in surface soils using Hg-MIF isotope

In this deposit, slightly negative or no Hg-MIF was observed for mineralized rocks ($\Delta^{199}\text{Hg}$: $-0.08 \pm 0.06\text{‰}$, 2SD, $n = 56$) and barren rocks ($\Delta^{199}\text{Hg}$: $-0.06 \pm 0.10\text{‰}$, 2SD, $n = 51$) in the Longtan Fm, whereas barren rocks from other strata showed slightly positive to no Hg-MIF ($\Delta^{199}\text{Hg}$: $0.06 \pm 0.10\text{‰}$, 2SD, $n = 62$) (Yin et al., 2019). And near-zero $\Delta^{199}\text{Hg}$ were observed in total gaseous mercury samples ($0.02 \pm 0.06\text{‰}$, 1SD, $n = 46$) in Guizhou province (Yu et al., 2016). However, significantly negative MIF has been observed in surface soils. $\Delta^{199}\text{Hg}$ values of all soils fluctuate between -0.33‰ and 0.03‰ , with an average of $-0.13 \pm 0.08\text{‰}$ ($n = 20$, 1SD) (Tables 1 and 4). The $\Delta^{199}\text{Hg}$ values show insignificant variation between the background (from -0.30‰ to 0.10‰) and deep ores-related (from -0.20‰ to 0.00‰) samples (Table 4; Fig. 4). Variations of soil $\Delta^{199}\text{Hg}$ can be explained by

the mixing of Hg input sources (weathered rocks, geogas, and atmospheric inputs) and surface processes (such as photochemical reactions) that fractionate Hg isotopes (e.g., Jiskra et al., 2017; Zheng et al., 2016). The latter, in this study, plays a more important role in changing soil MIF signatures because the $\Delta^{199}\text{Hg}$ values of all possible Hg input sources (Fig. 4) are near zero.

At least two mechanisms can explain MIF of ^{199}Hg and ^{201}Hg , namely the nuclear volume effect (NVE) (Schauble, 2007) and the magnetic isotope effect (MIE) (Buchachenko, 2001). The NVE mechanism can take place during processes like elemental $\text{Hg}(0)$ liquid-vapor equilibrium (Estrade et al., 2009; Ghosh et al., 2013), abiotic non-photochemical Hg (II) (aq) reduction (Zheng and Hintelmann, 2009, 2010a), and equilibrium HgII(aq) -thiol complexation (Wiederhold et al., 2010). The MIE is a kinetic fractionation that appears to occur primarily during photochemical radical pair reactions (Bergquist and Blum, 2007; Zheng and Hintelmann, 2009, 2010b). Theory and observations suggest that the NVE and MIE could be differentiated according to their $\Delta^{199}\text{Hg}/\Delta^{201}\text{Hg}$ ratios. Plotting $\Delta^{199}\text{Hg}$ versus $\Delta^{201}\text{Hg}$ reveals a significant difference for MIE ($\Delta^{199}\text{Hg}/\Delta^{201}\text{Hg}$: 1.0–1.3) versus that of NVE ($\Delta^{199}\text{Hg}/\Delta^{201}\text{Hg}$: >1.6). In terms of MIE, aqueous Hg (II) photoreduction processes in the presence of natural DOC are associated with $\Delta^{199}\text{Hg}/\Delta^{201}\text{Hg}$ ratios of 1.0 to 1.2 (Bergquist and Blum, 2007; Zheng and Hintelmann, 2009), whereas MeHg photodegradation results in a $\Delta^{199}\text{Hg}/\Delta^{201}\text{Hg}$ ratio of 1.36 (Bergquist and Blum, 2007).

All soils in our study have a $\Delta^{199}\text{Hg}/\Delta^{201}\text{Hg}$ ratio of 0.817 ± 0.382 (2SE) (Fig. 6), which was more likely to be caused by Hg (II) photoreduction. This result is consistent with previous observations of soil samples also collected in Guizhou province ($\Delta^{199}\text{Hg}/\Delta^{201}\text{Hg}$: ~1; Feng et al., 2013). Large variations of MIF with $\Delta^{199}\text{Hg}/\Delta^{201}\text{Hg}$ of ~1 have been observed in the modern environment on the global scale (e.g., soils/sediments, plants, coal, atmospheric Hg species, and precipitations) (e.g., Biswas et al., 2008; Feng et al., 2010; Gratz et al., 2010; Liu et al., 2011; Yin et al., 2014). Primordial Hg in weathered

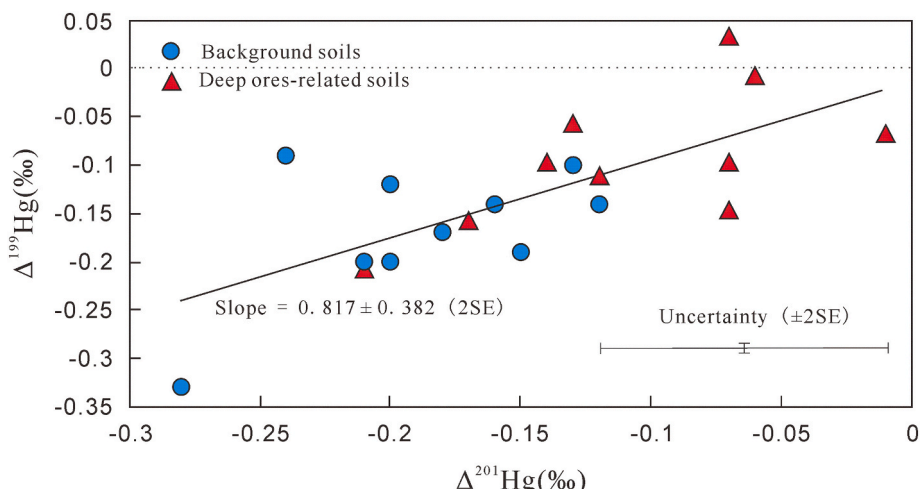


Fig. 6. Plot of $\Delta^{199}\text{Hg}$ versus $\Delta^{201}\text{Hg}$ for soils in the Nayang section of the Shuiyindong gold deposit. The regression line is calculated using the SPSS v17.0 statistical package (SPSS, Inc.).

rocks, geogas, and precipitation (Fig. 4) is characterized by $\Delta^{199}\text{Hg}$ of ~ 0 . However, once emitted to the surface environment, Hg(II) photo-reduction in aquatic ecosystems can imprint the Hg-MIF signature, leading to negative $\Delta^{199}\text{Hg}$ values in the product Hg(0). Thus, it is not feasible to apply Hg-MIF to trace the anomalous THg and TAu sources in topsoils in the Shuiyindong Au deposit.

5.4. How Hg and Au at depth penetrate to the surface

Hg-MDF ($\delta^{202}\text{Hg}$) could trace anomalous THg and TAu in topsoils from the deep mineralization in this deposit. However, the deep ore bodies under the A-B exploration line are located in the Upper Permian Longtan Fm at depths of 650 to 1200 m below the surface (Fig. 2). And it is necessary to discuss how Hg and Au related to the deep Au mineralization penetrate sedimentary cover (Fig. 2), several hundreds of meters thick, to the surface.

Firstly, the geochemical properties of these two elements determine that they are easy to migrate. Mercury is a semi-volatile metal element with a strong migration capability. Since the 1960s, the Hg anomaly in soil gas has been applied to explore hidden gold and base-metal deposits (McCarthy et al., 1969; McCarthy, 1972; Kromer et al., 1981; Carr et al., 1986; Fursov, 1990; Fedikow and Amor, 1990). For example, McCarthy et al. (1969) found Hg in soil-gas measurements outlined the disseminated gold deposit in bedrock at the Cortez mine in Nevada through as much as 30 m of gravel. Anomalous Hg in soil gas could be absorbed by organic matter, Fe-oxides/hydroxides, and clay minerals of the soils (Schuster, 1991; Yin et al., 1997), increasing Hg contents of topsoils. In the Qujia gold deposit, Shandong province, China, Wang et al. (2021) found that Hg can form high anomalies in the surface soil due to its high mobility, characterize transport channels, and serve as a pathfinder vectoring toward concealed ore bodies in the downward direction. In addition to vertical Hg migration from the deep ores to the surface, it is very likely that Hg also migrates laterally in the Shuiyindong deposit, owing to its strong mobility and the significant concentration difference between the mining and non-mining areas (Table 2). This is why the surface soils in this deposit have generally higher THg concentrations compared to its background range in Guizhou. However, the great contrast of THg between the background and deep ores-related samples (Table 2) indicates that much more Hg from the deep ore bodies still exist in the deep ores-related soils, and thus significantly influenced their Hg isotope composition. Therefore, the presence of lateral migration of Hg does not affect the trace of Hg anomalies on the surface using Hg-MDF isotopes.

Deformation of Au-bearing crystals at depth, such as pyrite, could

result in the formation of ultra-fine Au particles at micro- to nano-scale around the deep Au ore bodies (Li et al., 2020). Ultra-fine Au particles are mobile because they can be adsorbed onto the surfaces of geogas bubbles and migrate with the bubbles upwards to the surface (Wang et al., 1995, 1997). Arriving at the surface, Au particles could be trapped by Fe and Mn oxide coatings, clay minerals, colloids, soluble salts, and secondary carbonates in soils (Schuster, 1991; Wang et al., 1995, 1997; Yin et al., 1997). Ultra-fine gold particles in the surface media related to concealed gold deposits were observed in many previous studies (e.g., Cao et al., 2009; Cao, 2011; Hu and Cao, 2019; Lu et al., 2021; Ye et al., 2014).

Secondly, tectonic deformation in the strata above the ore bodies provides the migration pathway for these two elements. With the formation of macro-structures (Fig. 1), including the nearly E-W-trending Huijiabao anticline, two E-W reverse faults (F101 and F105), and a series of nearly S-N strike-slip faults, a large number of micro-fractures and cataclastic textures should also be widely developed in the rocks. They jointly provide migration channels for Au and Hg from the depth to the surface. Li et al. (2020) found gold filled in healed micro-fracture in the Jiaodong Au deposit by focused ion beam-scanning electron microscope (FIB-SEM) method, providing important evidence for geochemical exploration for concealed deposits based on nanoscale gold particles. Specifically, F101 does not cut through the deep gold ore bodies (Fig. 2). However, the anomalies of TAu and THg above the F101 are the most significant (Fig. 3). Because the fault is the main transport channel of ascending geogas, which can carry semi-volatile Hg and metallic nanoparticles (such as Au nanoparticles) from concealed ore bodies to the earth's surface (Han et al., 2009, 2015; Wang et al., 2006, 2021; Yang et al., 2015; Zhang et al., 2019). Therefore, semi-volatile Hg and ultra-fine Au particles are mobile and could continuously migrate from the depth to the surface through macro-structures, such as F101 in Fig. 2, and micro-fractures with the ascending geogas, then most of them are absorbed by the surface soils.

5.5. Implications for mineral exploration of concealed gold deposits

This study showed that Au and Hg could penetrate the sedimentary cover to the surface and it is possible to target the concealed gold deposit with a depth of more than 650 m using TAu and THg of the surface soils. Compared to TAu, THg has a better effect in indicating deep concealed Au deposit in this study (Table 2; Fig. 3). Although Hg is a traditional pathfinder element for Au deposit (Adepoju, 2019; Hedenquist et al., 2000; Korshunova and Charykova, 2019; McCarthy, 1972; Sadeghi et al., 2015; Varekamp and Buseck, 1984; Wang et al., 2021; Yalali-

Abanuz et al., 2012), previous studies stated that Hg anomalies are not necessarily connected with ore bodies (except for Hg ore bodies), because they could also be produced by structural activities without metallogenesis (Chen, 1997; Kodosky, 1989; Wang et al., 2006; Yang et al., 2015) and geothermal processes (Van Kooten, 1987). However, in this study, THg and TAu in surface soils are closely related (Table 3; Fig. 3) and Hg-MDF ($\delta^{202}\text{Hg}$) could trace anomalous Hg sources in topsoils from the deep mineralization. Thus, the Hg anomalies in the topsoils are closely connected with the deep gold mineralization in this deposit. Compared to other traditional pathfinder elements of Au deposits, such as As, Sb, and Tl, Hg is gaseous under high-temperature conditions at depth. It could quickly migrate along the pathway, travel longer distances, and indicate deeper ore bodies. Meanwhile, high-precision analytical methods for Hg isotope compositions have been established and Hg-MDF and Hg-MIF could provide multidimensional information about the sources and fates of Hg in the environment. Overall, in addition to THg of the surface soils, Hg-MDF is suggested to apply as a new exploration vector in the exploration tool kit of Au explorers globally.

6. Conclusions

This study collected surface soil samples over the concealed Shuiyindong Au deposit, analyzed their TAu, and THg contents, and Hg isotope compositions, and discern whether Hg isotopes could trace the sources of TAu anomalies in the surface soil samples. Based on the above discussion, we can draw the following conclusions:

- 1) The change trends of TAu and THg along the exploration line are relatively consistent. The anomalies of TAu and THg are obvious in the deep ores-related soils. Their median, AM, and GM of TAu are 1.59, 1.70, and 1.69 times those in the background soils, respectively. And these figures for THg are 6.13, 7.08, and 6.61, respectively.
- 2) $\delta^{202}\text{Hg}$ values in background soils ($-1.67\text{\textperthousand}$ to $-0.66\text{\textperthousand}$, averaging $-1.07 \pm 0.28\text{\textperthousand}$, $n = 10$, 1SD) are obviously lower than deep ores-related soils ($-0.78\text{\textperthousand}$ to $-0.23\text{\textperthousand}$, averaging $-0.46 \pm 0.19\text{\textperthousand}$, $n = 10$, 1SD). However, there is no clear difference in $\Delta^{199}\text{Hg}$ between background soils and deep ores-related soils.
- 3) $\delta^{202}\text{Hg}$ and $1/\text{THg}$ in deep ores-related soils have been altered by the ascending geogas from the mineralized rocks of the Longtan Fm. Hg-MDF ($\delta^{202}\text{Hg}$) could trace anomalous Hg and Au sources in topsoils from the deep Au ore bodies in this study. However, it is not feasible to apply Hg-MIF to trace the anomalous Au sources in topsoils, because Hg(II) photoreduction can imprint the Hg-MIF signature, leading to negative $\Delta^{199}\text{Hg}$ values.
- 4) Semi-volatile Hg and ultra-fine Au particles are mobile and could continuously migrate from the depth to the surface through macrostructures and micro-fractures with the ascending geogas, then most of them are absorbed by the surface soils.

Overall, this study successfully traced the concealed gold mineralization with a depth of more than 650 m using $\delta^{202}\text{Hg}$, which is significant for mineral exploration of deep-seated Au deposits.

CRediT authorship contribution statement

Xuemin Liu led the project. Xuemin Liu, Feilin Zhu, Qinping Tan, Yue Yufan, and Li Chen collected the samples. Shuting Liu and Lin Wang prepared, analyzed samples, and interpreted the data. Xuemin Liu, Feilin Zhu, and Shuting Liu wrote this manuscript.

Declaration of competing interest

The authors declare that they have no known competing financial interests or personal relationships that could have appeared to influence

the work reported in this paper.

Acknowledgments

The results were supported by the National Key Research Project (2016YFC0600604). Many thanks are given to all participants in field sampling, laboratory analysis, and data processing. We also thank the reviewers and editors for their thorough work and very helpful comments on prior versions of this paper. All of these supportive efforts are acknowledged here with appreciation.

References

- Adepoju, M.O., 2019. Identifying pathfinder elements for gold in soil geochemical data from a part of Igara Schist belt, southwestern Nigeria: a multivariate statistical approach. *Geoscience Bulletin* 1, 1–8.
- An, Z., Kutzbach, J.E., Prell, W.L., Porter, S.C., 2001. Evolution of Asian monsoons and phased uplift of the Himalayan: Tibetan plateau since late Miocene times. *Nature* 411, 62–66.
- Anand, R.R., Aspandiar, M.F., Noble, R.R.P., 2016. A review of metal transfer mechanisms through transported cover with emphasis on the vadose zone within the Australian regolith. *Ore Geol. Rev.* 73, 394–416.
- Anunziatellis, A., Ciotoli, G., Lombardia, S., Nolasco, F., 2003. Short- and long-term gas hazard: the release of toxic gases in the Alban Hills volcanic area (central Italy). *J. Geochem. Explor.* 77, 93–108.
- Aspandiar, M.F., Anand, R.R., Gray, D.G., 2006. Geochemical dispersion mechanisms through transported cover: implications for mineral exploration in Australia, 84 pp. In: CRCLEME Restricted Report, 230. Reissued as open File Report 246, Perth, 2008.
- Bergquist, B.A., Blum, J.D., 2007. Mass-dependent and mass-independent fractionation of Hg isotopes by photoreduction in aquatic systems. *Science* 318, 417–420.
- Biswas, A., Blum, J.D., Bergquist, B.A., Keeler, G.J., Xie, Z., 2008. Natural mercury isotope variation in coal deposits and organic soils. *Environ. Sci. Technol.* 42, 8303–8309.
- Blum, J.D., Bergquist, B.A., 2007. Reporting of variations in the natural isotopic composition of mercury. *Anal. Bioanal. Chem.* 388, 353–359.
- Blum, J.D., Sherman, L.S., Johnson, M.W., 2014. Mercury isotopes in Earth and environmental sciences. *Annu. Rev. Earth Planet. Sci.* 42, 249–269.
- Braxton, D., Mathur, R., 2011. Exploration applications of copper isotopes in the supergene environment: a case study of the Bayugao Porphyry Copper Gold Deposit, Southern Philippines. *Econ. Geol.* 106, 1447–1463.
- Brennecke, G.A., Borg, L.E., Hutcheon, I.D., Sharp, M.A., Anbar, A.D., 2010. Natural variations in uranium isotope ratios of uranium ore concentrates: understanding the 238U/235U fractionation mechanism. *Earth Planet. Sci. Lett.* 291, 228–233.
- Buchachenko, A.L., 2001. Magnetic isotope effect: nuclear spin control of chemical reactions. *J. Phys. Chem. A* 105, 9995–10011.
- Cameron, E.M., Hamilton, S.M., Leybourne, M.I., Hall, G.E.M., McLenaghan, M.B., 2004. Finding deeply buried deposits using geochemistry. *Geochem. Explor. Environ. Anal.* 4, 7–32.
- Cao, J., 2011. Migration mechanisms of gold nanoparticles explored in geogas of the Hetai ore district, southern China. *Geochem. J.* 45 (3), e9–e13.
- Cao, J., Hu, R., Liang, Z., Peng, Z., 2009. TEM observation of geogas-carried particles from the Changkeng concealed gold deposit, Guangdong Province, South China. *J. Geochem. Explor.* 101 (3), 247–253.
- Carr, G.R., Wilmshurst, J.R., Ryall, W.R., 1986. Evaluation of mercury pathfinder techniques: base metal and uranium deposits. *J. Geochem. Explor.* 26, 1–117.
- Chardon, D., Grimaud, J.L., Beauvais, A., Bamba, O., 2018. West african lateritic pediments: landform-regolith evolution processes and mineral exploration pitfalls. *Earth Sci. Rev.* 179, 124–146.
- Chen, J., 1997. Elementary analysis of relationship between mercury anomaly of fault product gas and active fault. *Crustal Deformation Earthq.* 17 (2), 97–100.
- Cheng, Q., 2007. Mapping singularities with stream sediment geochemical data for prediction of undiscovered mineral deposits in Gejiu, Yunnan Province, China. *Ore Geol. Rev.* 32, 314–324.
- Clarke, J.R., Meier, A.L., 1990. Enzyme leaching of surficial geochemical samples for detecting hydromorphic trace-element anomalies associated with precious metal mineralized bedrock buried beneath glacial overburden in northern Minnesota. In: Proceedings of the Gold' 90 Symposium—Gold' 90, Salt Lake City, UT, USA, 26 February–1 March 1990, pp. 189–207.
- Cohen, D.R., Kelley, D.L., Anand, R., Coker, W.B., 2010. Major advances in exploration geochemistry, 1998–2007. *Geochem. Explor. Environ. Anal.* 10, 3–16.
- de Caritat, P., Main, P.T., Grunsky, E.C., Mann, A.W., 2016. Recognition of geochemical footprints of mineral systems in the regolith at regional to continental scales. *J. Earth Sci.* 64, 1033–1043.
- Demers, J.D., Blum, J.D., Zak, D.R., 2013. Mercury isotopes in a forested ecosystem: implications for air-surface exchange dynamics and the global mercury cycle. *Glob. Biogeochem. Cycl.* 27, 222–238.
- Estrade, N., Carignan, J., Sonke, J.E., Donard, O.F.X., 2009. Mercury isotope fractionation during liquid-vapor evaporation experiments. *Geochim. Cosmochim. Acta* 73, 2693–2711.
- Fedikow, M.A.F., Amor, S.D., 1990. Evaluation of a mercury vapour detection system in base- and precious-metal exploration, northern Manitoba. *J. Geochem. Explor.* 38, 351–374.

- Feng, X., Foucher, D., Hintelmann, H., Yan, H., He, T., Qiu, G., 2010. Tracing mercury contamination sources in sediments using mercury isotope compositions. *Environ. Sci. Technol.* 44, 3363–3368.
- Feng, X., Yin, R., Yu, B., Du, B., 2013. Mercury isotope variations in surface soils in different contaminated areas in Guizhou Province, China. *Chin. Sci. Bull.* 58, 249–255.
- Fursov, V.Z., 1990. Mercury vapour survey: technique and results. *J. Geochem. Explor.* 38, 145–155.
- Ghosh, S., Schauble, E.A., Couloume, G.L., Blum, J.D., Bergquist, B.A., 2013. Estimation of nuclear volume dependent fractionation of mercury isotopes in equilibrium liquid-vapor evaporation experiments. *Chem. Geol.* 336, 5–12.
- Gold, T., Soter, S., 1980. The deep earth-gas hypothesis. *Sci. Am.* 242, 132–138.
- González-Álvarez, I., Boni, M., Anand, R.R., 2016. Mineral exploration in regolith dominated terrains: global considerations and challenges. *Ore Geol. Rev.* 73, 375–379.
- González-Álvarez, I., Goncalves, M.A., Carranza, E.J.M., 2020. Challenges for mineral exploration in the 21st century: targeting mineral deposits under cover. *Ore Geol. Rev.* 103785.
- Gratz, L.E., Keeler, G.J., Blum, J.D., Sherman, L.S., 2010. Isotopic composition and fractionation of mercury in great lakes precipitation and ambient air. *Environ. Sci. Technol.* 44, 7764–7770.
- Grunsky, E.C., de Caritat, P., 2019. State-of-the-art analysis of geochemical data for mineral exploration. *Geochim. Explor. Environ. Anal.* 20, 217–232.
- Gu, W., Hao, X., Wang, Z., Zhang, J., Huang, L., Pei, S., 2020. Ethnobotanical study on medicinal plants from the Dragon Boat Festival herbal markets of Qianxinan, southwestern Guizhou, China. *Plant Divers.* 42 (6), 427–433.
- Guo, Z.T., Ruddiman, W.F., Hao, Q.Z., Wu, H.B., Qiao, Y.S., Zhu, R.X., Peng, S.Z., Wei, J.J., Yuan, B.Y., Liu, T.S., 2002. Onset of Asian desertification by 22 Myr ago inferred from loess deposits in China. *Nature* 416, 159–163.
- Han, R., Ma, D., Wu, P., Ma, G., 2009. Ore-finding method of fault tectono-geochemistry in the Tongchang Cu–Au polymetallic orefield, Shaanxi, China: I. Dynamics of tectonic ore-forming processes and prognosis of concealed ores. *Chin. J. Geochim.* 28 (4), 397–404.
- Han, R., Chen, J., Wang, F., Wang, X., Li, Y., 2015. Analysis of metal-element association halos within fault zones for the exploration of concealed ore-bodies - a case study of the Qinling-Zn-Pb-(Ag-Ge) deposit in the Huize mine district, northeastern Yunnan, China. *J. Geochem. Explor.* 159, 62–78.
- Hedenquist, J.W., Arribas, A.R., Gonzalez-Urrien, E., 2000. Exploration for epithermal gold deposits. In: Hagemann, S.G., Brown, P.E. (Eds.), *Gold in 2000, Reviews in Economic Geology*, 13, pp. 45–77.
- Hu, G., Cao, J., 2019. Occurrence and significance of natural ore-related Ag nanoparticles in groundwater systems. *Chem. Geol.* <https://doi.org/10.1016/j.chemgeo.2019.03.036>.
- Jiskra, M., Wiederhold, J.G., Skyllberg, U., Kronberg, R.-M., Kretzschmar, R., 2017. Source tracing of natural organic matter bound mercury in boreal forest runoff with mercury stable isotopes. *Environ Sci Process Impacts* 19 (10), 1235–1248.
- Keegan, E., Richter, S., Kelly, I., Wong, H., Gadd, P., Kuehn, H., Alonso-Munoz, A., 2008. The provenance of Australian uranium ore concentrates by elemental and isotopic analysis. *Appl. Geochem.* 23, 765–777.
- Kelley, D.L., 2003. The use of partial extraction geochemistry for copper exploration in northern Chile. *Geochim. Explor. Environ. Anal.* 3, 85–104.
- Kelley, D.L., Kelley, K.D., Coker, W.B., Cauglin, B., Doherty, M., 2006. Beyond the obvious limits of ore deposits: the use of mineralogical, geochemical and biological features for the remote detection of mineralization. *Econ. Geol.* 101, 729–752.
- Kidder, J.A., Voinot, A., Sullivan, K.V., Chipley, D., Valentino, M., Layton-Matthews, D., Leybourne, M., 2020. Improved ion-exchange column chromatography for Cu purification from high-Na matrices and isotopic analysis by MC-ICP-MS. *J. Anal. At. Spectrom.* <https://doi.org/10.1039/c9ja00359b>.
- Kodosky, L.G., 1989. Surface mercury geochemistry as a guide to volcanic vent structure and zones of high heat flow in the Valley of ten Thousand Smokes, Katmai National Park, Alaska. *J. Volcanol. Geotherm. Res.* 38 (3), 227–242.
- Korshunova, V.A., Charykova, M.V., 2019. Mobile forms of gold and pathfinder elements in surface sediments at the Novye Peski gold deposit and in the Piilola prospecting area (Karelia Region). *Minerals* 9, 34.
- Kromer, E., Griedrich, G., Wallner, P., 1981. Mercury and mercury compounds in surface air, soil gas, soils and rocks. *J. Geochem. Explor.* 15, 51–62.
- Kyser, T.K., Leybourne, M.I., Layton-Matthews, D., 2020. Advances in the use of isotopes in geochemical exploration: instrumentation and applications in understanding geochemical processes. *Geochim. Explor. Environ. Anal.* <https://doi.org/10.1144/geoch2019-045>.
- Li, J.W., Vasconcelos, P., Duzgoren-Aydin, N., Yan, D.R., Zhang, W., Deng, X.D., Zhao, X. F., Zeng, Z.P., Hu, M.A., 2007. Neogene weathering and supergene manganese enrichment in subtropical South China: an 40Ar/39Ar approach and paleoclimatic significance. *Earth Planet. Sci. Lett.* 256, 389–402.
- Li, R., Wang, X., Yang, L., Zhang, B., Liu, Q., Liu, D., 2020. The characteristic of microstructural deformation of gold bearing pyrite in Jiaodong: the links between nanoscale gold enrichment and crystal distortion. *Ore Geol. Rev.* 103495.
- Liang, J., Li, J., Liu, X., Zhai, W., Huang, Y., Zhao, J., Sun, W., Song, M., Li, J., 2020. Multiple element mapping and in-situ S isotopes of Au-carrying pyrite of Shuiyindong gold deposit, southwestern China using NanoSIMS: Constraints on Au sources, ore fluids, and mineralization processes. *Ore Geol. Rev.* 123, 103576.
- Lintern, M., Anand, R., Ryan, C., Paterson, D., 2013. Natural gold particles in Eucalyptus leaves and their relevance to exploration for buried gold deposits. *Nat. Commun.* 4, 2614.
- Liu, J., 2001. The geology of the Yanshang gold deposit, Zhenfeng county, Guizhou. *Guizhou Geol.* 18 (3), 174–178 (in Chinese with English abstract).
- Liu, R.X., Wang, Z.H., Zhang, Z.H., 2009. Ecological characteristics of bryophyte communities from Karst rock desertification peak cluster in Zhenfeng of Guizhou Province. *Bull. Bot. Res.* 29, 734–741.
- Liu, J., Feng, X., Yin, R., Zhu, W., Li, Z., 2011. Mercury distributions and mercury isotope signatures in sediments of Dongjiang River, the Pearl River Delta, China. *Chem. Geol.* 287, 81–89.
- Liu, J., Xia, Y., Tao, Y., Yang, C., Wang, Z., Tan, Q., Fu, S., Chen, R., Wu, W., 2014. The relation between SBT and gold-antimony deposit metallogenesis and prospecting in Southwest Guizhou. *Guizhou Geol.* 31 (4), 267–272 (in Chinese with English abstract).
- Liu, J., Yang, C., Wang, Z., Wang, D., Qi, L., Li, J., Hu, C., Xu, L., 2017. Geological research of Shuiyindong gold deposit in Zhenfeng County, Guizhou Province (2). In: Geological Survey of China, 42, pp. 32–41 (in Chinese with English abstract).
- Lougheed, D.H., McClenaghan, M.B., Layton-Matthews, D., Leybourne, M., 2020. Exploration potential of fine-fraction heavy mineral concentrates from till using automated mineralogy: A case study from the Izok Lake Cu-Zn-Pb-Ag VMS Deposit, Nunavut, Canada. *Minerals* 10, 310.
- Lu, M., Cao, J., Liu, X., Qiu, J., 2021. Nanoparticles in various media on surfaces of ore deposits: Study of the more than 1000 m deep concealed Shaling gold deposit. *Ore Geol. Rev.* 139, 104466.
- Malmqvist, L., Kristiansson, K., 1984. Experiment evidence for an ascending micro-flow of geogas in the ground. *Earth Planet. Sci. Lett.* 70, 407–416.
- Mann, A.W., Birrell, R.D., Mann, A.T., Humphreys, D.B., Perdris, J.L., 1998. Application of the mobile metal ion technique to routine geochemical exploration. *J. Geochem. Explor.* 61, 87–102.
- Mathur, R., Titley, S., Barra, F., Brantley, S., Wilson, M., Phillips, A., Munizaga, F., Maksaev, V., Vervoort, J., Hart, G., 2009. Exploration potential of Cu isotope fractionation in porphyry copper deposits. *J. Geochem. Explor.* 102, 1–6.
- Mathur, R., Titley, S.R., Schlitt, W.J., Wilson, M., 2012. Cu isotope fractionation in: exploration geology and hydrometallurgy: examples from porphyry copper deposits. *Min. Eng.* 64, 42–46.
- McCarthy Jr., J.H., 1972. Mercury vapor and other volatile components in the air as guides to ore deposits. *J. Geochem. Explor.* 1, 143–162.
- McCarthy Jr., J.H., Vaughn Jr., W.W., Learned Jr., R.E., Meuschke Jr., J.L., 1969. Mercury in Soil Gas and Air—A Potential Tool in Mineral Exploration (No. 609). US Geological Survey.
- Momo, M.N., Beauvais, A., Tematio, P., Ambrosi, J.P., Yemefack, M., Yerima, B.P.K., Yongue-Fouateu, R., 2019. Lateritic weathering of trachyte, and bauxite formation in West Cameroon: morphological and geochemical evolution. *J. Geochem. Explor.* 205, 106324.
- Morner, N.A., Etiöpe, G., 2002. Carbon degassing from the lithosphere. *Glob. Planet. Chang.* 33, 185–203.
- Rantitsch, G., 2001. The fractal properties of geochemical landscapes as an indicator of weathering and transport processes within the Eastern Alps. *J. Geochem. Explor.* 73, 27–42.
- Sadeghi, M., Billay, A., Carranza, E.J.M., 2015. Analysis and mapping of soil geochemical anomalies: implications for bedrock mapping and gold exploration in Giyani area, South Africa. *J. Geochem. Explor.* 154, 180–193.
- Schauble, E.A., 2007. Role of nuclear volume in driving equilibrium isotope fractionation of mercury, thallium, and other very heavy elements. *Geochim. Cosmochim. Acta* 71, 2170–2189.
- Schuster, E., 1991. The behavior of mercury in the soil with special emphasis on complexation and adsorption processes: a review of the literature. *Water Air Soil Pollut.* 56, 667–680.
- Sherman, L.S., Blum, J.D., Nordstrom, D.K., McCleskey, R.B., Barkay, T., Vetriani, C., 2009. Mercury isotopic composition of hydrothermal systems in the Yellowstone Plateau volcanic field and Guaymas Basin sea-floor rift. *Earth Planet. Sci. Lett.* 29, 86–96.
- Smith, C.N., Kesler, S.E., Klaue, B., Blum, J.D., 2005. Mercury isotope fractionation in fossil hydrothermal systems. *Geology* 33, 825–828.
- Smith, C.N., Kesler, S.E., Blum, J.D., Ryuba, J.J., 2008. Isotope geochemistry of mercury in source rocks, mineral deposits and spring deposits of the California Coast Ranges, USA. *Earth Planet. Sci. Lett.* 269, 399–407.
- Sonke, J.E., Schaefer, J., Chmeleff, J., Audry, S., Blanc, G., Dupré, B., 2010. Sedimentary mercury stable isotope records of atmospheric and riverine pollution from two major European heavy metal refineries. *Chem. Geol.* 279, 90–100.
- Spadoni, M., 2006. Geochemical mapping using a geomorphologic approach based on catchments. *J. Geochem. Explor.* 90, 183–196.
- Su, W., Xia, B., Zhang, H., Zhang, X., Hu, R., 2008. Visible gold in arsenian pyrite at the Shuiyindong Carlin-type gold deposit, Guizhou, China: implications for the environment and processes of ore formation. *Ore Geology Review* 33 (3), 667–679.
- Su, W., Hu, R., Xia, B., Xia, Y., Liu, Y., 2009. Calcite Sm-Nd isochron age of the Shuiyindong Carlin-type gold deposit, Guizhou, China. *Chem. Geol.* 258, 269–274.
- Su, W., Zhang, H., Hu, R., Ge, X., Xia, B., Chen, Y., Zhu, C., 2012. Mineralogy and geochemistry of gold-bearing arsenian pyrite from the Shuiyindong Carlin-type gold deposit, Guizhou, China: implications for gold depositional processes. *Mineral. Deposita* 47 (6), 653–662.
- Sun, X.J., Wang, P.X., 2005. How old is the Asian monsoon system? Palaeobotanical records from China. *Palaeogeogr. Palaeoclimatol. Palaeoecol.* 222, 181–222.
- Sun, R., Heimburger, L.E., Sonke, J.E., Liu, G., Amouroux, D., Berail, S., 2013. Mercury stable isotope fractionation in six utility boilers of two large coal-fired power plants. *Chem. Geol.* 336, 103–111.
- Tan, Q., Xia, Y., Xie, Z., Yan, J., 2015a. Migration paths and precipitation mechanisms of ore-forming fluids at the Shuiyindong Carlin-type gols deposit, Guizhou, China. *Ore Geol. Rev.* 69, 140–156.

- Tan, Q., Xia, Y., Xie, Z., Yan, J., Wei, D., 2015b. S, C, O, H, and Pb isotope studies for the Shuiyindong Carlin-type gold deposit, Southwest Guizhou, China: constrains for ore genesis. *Chin. J. Geochem.* 34 (4), 525–539 (in Chinese with English abstract).
- Tan, Q., Xia, Y., Wang, X., Xie, Z., Wei, D., 2017. Carbon-oxygen isotopes and rare earth elements as an exploration vector for Carlin-type gold deposits: a case study of the Shuiyindong gold deposit, Guizhou Province, SW China. *J. Asian Earth Sci.* 148, 1–12.
- Tan, Q., Xia, Y., Xie, Z., Wang, Z., Wei, D., Zhao, T., Yan, Li, S., 2019. Two hydrothermal events at the Shuiyindong Carlin-type gold deposit in Southwestern China: insight from Sm–Nd dating of fluorite and calcite. *Minerals* 9 (4), 230.
- Tong, C., Li, J., Ge, L., Yang, F., 1998. Experimental observation of the nano-scale particles in geogas matters and its geological significance. *Sci. China Ser. D* 41, 325–329.
- Uvarova, Y.A., Kyser, T.K., Geagea, M.L., Chipley, D., 2014. Variations in the uranium isotopic compositions of uranium ores from different types of uranium deposits. *Geochim. Cosmochim. Acta* 146, 1–17.
- Van Kooten, G.K., 1987. Geothermal exploration using surface mercury geochemistry. *J. Volcanol. Geotherm. Res.* 31 (3), 269–280.
- Varekamp, J.C., Buseck, P.R., 1984. The speciation of mercury in hydrothermal systems, with applications to ore deposition. *Geochim. Cosmochim. Acta* 48, 177–185.
- Wang, X., 1998. Leaching of mobile forms of metals in overburden: development and application. *J. Geochem. Explor.* 61, 39–55.
- Wang, J., Zuo, R., 2020. Assessing geochemical anomalies using geographically weighted lasso. *Appl. Geochim.* 119, 104668.
- Wang, X., Xie, X., Ye, S., 1995. Concepts for gold exploration based on the abundance and distribution of ultrafine gold. *J. Geochem. Explor.* 55 (1–3), 93–102.
- Wang, X., the CGB Sampling Team, 2015. China geochemical baselines: sampling methodology. *J. Geochem. Explor.* 148, 25–39.
- Wang, X., Cheng, Z., Lu, Y., Li, X., Xie, X., 1997. Nanoscale metals in earthgas and mobile forms of metals in overburden in wide-spaced regional exploration for giant ore deposits in overburden terrains. *J. Geochem. Explor.* 58, 63–72.
- Wang, G., Liu, C., Wang, J., Liu, W., Zhang, P., 2006. The use of soil mercury and radon gas surveys to assist the detection of concealed faults in Fuzhou City, China. *Environ. Geol.* 51 (1), 83–90.
- Wang, X., Wen, X., Rong, Y., Liu, Z., Sun, B., Zhao, S., Shi, S., Wei, H., 2007. Vertical variations and dispersion of elements in arid desert regolith: a case study from the Jinwozi gold deposit, northwestern China. *Geochem. Explor. Environ. Anal.* 7 (2), 163–171.
- Wang, X., Liu, X., Han, Z., Zhou, J., Xu, S., Zhang, Q., Chen, H., Bo, W., Xia, X., 2015. Concentration and distribution of mercury in drainage catchment sediment and alluvial soil of China. *J. Geochem. Explor.* 154, 32–48.
- Wang, X., Zhang, B., Lin, X., Xu, S., Yao, W., Ye, R., 2016. Geochemical challenges of diverse regolith-covered terrains for mineral exploration in China. *Ore Geol. Rev.* 73, 417–431.
- Wang, Q., Yang, L., Xu, X., Santosh, M., Wang, Y., Wang, T., Chen, F., Wang, R., Gao, L., Liu, X., Yang, S., Zeng, Y., Chen, J., Zhang, Q., Deng, J., 2020. Multi-stage tectonics and metallogeny associated with phanerozoic evolution of the South China block: a holistic perspective from the Youjiang basin. *Earth Sci. Rev.* 211, 103405.
- Wang, Q., Wang, X., Liu, H., Tian, M., Zhang, B., Li, R., Yang, D., Xiong, Y., 2021. Targeting deep-seated gold deposits: a study from the Qujia gold deposit, Shandong province, China. *Appl. Geochim.* 130, 104982.
- Wiederhold, J.G., Cramer, C.J., Daniel, K., Infante, I., Bourdon, B., Kretzchmar, R., 2010. Equilibrium mercury isotope fractionation between dissolved Hg(II) species and thiol-bound Hg. *Environ. Sci. Technol.* 44, 4191–4197.
- Xia, Y., 2005. Characteristics and Model for Shuiyindong Gold Deposit in Southwestern Guizhou, China. Institute of Geochemistry, Chinese Academy of Sciences. Unpublished Ph.D. thesis.
- Xu, C., Yin, R., Peng, J., Hurley, J.P., Lepak, R.F., Gao, J.F., Feng, X., Hu, R., Bi, X., 2018. Mercury isotope constraints on the source for sediment-hosted lead-zinc deposits in the Changdu area, southwestern China. *Mineral. Deposita* 53, 339–352.
- Yan, M., Wang, C., Cao, X., Gu, X., Chi, H., 1995. Eleven gold geochemical reference samples (GAu 8–18). *Geostand. Geoanal. Res.* 19 (2), 125–133.
- Yang, D., Zhang, L., Liu, Y., Ren, H., Xie, F., Chen, G., 2015. Mercury indicating inflow zones and ruptures along the Wenchuan Ms 8.0 earthquake fault. *Chin. J. Geochem.* 34 (2), 201–207.
- Yaylali-Abanuz, G., Tüysüz, N., Akaryali, E., 2012. Soil geochemical prospecting for gold deposit in the Arzular area (NE Turkey). *J. Geochem. Explor.* 112, 107–117.
- Ye, R., Wang, X.Q., Zhang, B.M., 2014. Microscopic and nanoscale understanding of formation of gold geochemical provinces. *Acta Geol. Sin.* 88 (3), 801–809.
- Yin, Y., Allen, E., Huang, C.P., Sanders, P.F., 1997. Adsorption/desorption isotherms of Hg (II) by soil. *Soil Sci.* 162, 35–45.
- Yin, R., Feng, X., Shi, W., 2010. Application of the stable isotope system to the study of sources and fate of Hg in the environment: a review. *Appl. Geochem.* 25, 1467–1477.
- Yin, R., Feng, X., Wang, J., Bao, Z., Yu, B., Chen, J., 2013. Mercury isotope variations between bioavailable mercury fractions and total mercury in mercury contaminated soil in Wanshan Mercury Mine, SW China. *Chem. Geol.* 336, 80–86.
- Yin, R., Feng, X., Chen, J., 2014. Mercury stable isotopic compositions in coals from major coal producing fields in China and their geochemical and environment implications. *Environ. Sci. Technol.* 48, 5565–5574.
- Yin, R., Feng, X., Hurley, J.P., Krabbenhoft, D.P., Lepak, R.F., Hu, R., Zhang, Q., Li, Z., Bi, X., 2016a. Mercury isotopes as proxies to identify sources and environmental impacts of mercury in sphalerites. *Sci. Rep.* 6, 18686.
- Yin, R., Krabbenhoft, D.P., Bergquist, B.A., Zheng, W., Lepak, R.F., Hurley, J.P., 2016b. Effects of mercury and thallium concentrations on high precision determination of mercury isotopic composition by Neptune Plus multiple collector inductively coupled plasma mass spectrometry. *J. Anal. At. Spectrom.* 31, 2060–2068.
- Yin, R., Deng, C., Lehmann, B., Sun, G., Lepak, R.F., Hurley, J.P., Zhao, C., Xu, G., Tan, Q., Xie, Z., Hu, R., 2019. Magmatic-hydrothermal origin of mercury in carlin-style and epithermal gold deposits in China: evidence from mercury stable isotopes. *ACS Earth Space Chem.* 3 (8), 1631–1639.
- Yousefi, M., Carranza, E.J.M., Kamkar-Rouhani, A., 2013. Weighted drainage catchment basin mapping of geochemical anomalies using stream sediment data for mineral potential modeling. *J. Geochem. Explor.* 128, 88–96.
- Yu, B., Fu, X., Yin, R., Zhang, H., Wang, X., Lin, C.-J., Wu, C., Zhang, Y., He, N., Fu, P., Wang, Z., Shang, L., Sommar, J., Snoke, J.E., Maurice, L., Guinot, B., Feng, X., 2016. Isotopic composition of atmospheric mercury in China: new evidence for sources and transformation processes in air and in vegetation. *Environ. Sci. Technol.* 50, 9262–9269.
- Zerkle, A.L., Yin, R., Chen, C., Li, X., Izon, G.J., Grasby, S.E., 2020. Anomalous fractionation of mercury isotopes in the late Archean atmosphere. *Nat. Commun.* 11, 1709.
- Zhang, B., Wang, X., Ye, R., Zhou, J., Liu, H., Liu, D., Han, Z., Lin, X., Wang, Z., 2015. Geochemical exploration for concealed deposits at the periphery of the Zijinshan copper-gold mine, southeastern China. *J. Geochem. Explor.* 157, 184–193.
- Zhang, B., Han, Z., Wang, X., Liu, H., Wu, H., Feng, H., 2019. Metal-bearing nanoparticles observed in soils and fault gouges over the Shenjiayao gold deposit and their significance. *Minerals* 9, 414.
- Zheng, W., Hintelmann, H., 2009. Mercury isotope fractionation during photoreduction in natural waters is controlled by its Hg/DOC ratio. *Geochim. Cosmochim. Acta* 73, 6704–6715.
- Zheng, W., Hintelmann, H., 2010a. Nuclear field shift effect in isotope fractionation of mercury during abiotic reduction in the absence of light. *J. Phys. Chem. A* 114, 4238–4245.
- Zheng, W., Hintelmann, H., 2010b. Isotope fractionation of mercury during its photochemical reduction by low-molecular weight organic compounds. *J. Phys. Chem. A* 114, 4246–4253.
- Zheng, W., Obrist, D., Weis, D., Bergquist, B.A., 2016. Mercury isotope compositions across North American forests. *Glob. Biogeochem. Cycl.* 30 (10), 1475–1492.